Lab on a Chip

PAPER

View Article Online
View Journal

Cite this: DOI: 10.1039/d4lc00736k

Large-scale acoustic single cell trapping and selective releasing†

Xiang Zhang,[a] Jacob Smith,[a] Amanda Chengyi Zhou,[e] Jacqueline Thuy-Tram Duong,[b] Tong Qi,[cd] Shilin Chen,[cd] Yen-Ju Lin,[b] Alexi Gill,[a] Chih-Hui Lo,[e] Neil Y. C. Lin,[aef] Jing Wen,[d] Yunfeng Lu[c] and Pei-Yu Chiou*[a]

Received 4th September 2024,
Accepted 15th January 2025

DOI: 10.1039/d4lc00736k

rsc.li/loc

Recent advancements in single-cell analysis have underscored the need for precise isolation and manipulation of individual cells. Traditional techniques for single-cell manipulation are often limited by the number of cells that can be parallel trapped and processed and usually require complex devices or instruments to operate. Here, we introduce an acoustic microfluidic platform that efficiently traps and selectively releases individual cells using spherical air cavities embedded in a polydimethylsiloxane (PDMS) substrate for large scale manipulation. Our device utilizes the principle of acoustic impedance mismatches to generate near-field acoustic potential gradients that create trapping sites for single cells. These single cell traps can be selectively disabled by illuminating a near-infrared laser pulse, allowing targeted release of trapped cells. This method ensures minimal impact on cell viability and proliferation, making it ideal for downstream single-cell analysis. Experimental results demonstrate our platform's capability to trap and release synthetic microparticles and biological cells with high efficiency and biocompatibility. Our device can handle a wide range of cell sizes (8–30 μm) across a large active manipulation area of 1 cm^2 with 20 000 single-cell traps, providing a versatile and robust platform for single-cell applications. This acoustic microfluidic platform offers a cost-effective and practical method for large scale single-cell trapping and selective releasing with potential applications in genomics, proteomics, and other fields requiring precise single-cell manipulation.

Introduction

Recent studies have highlighted the significant heterogeneity present in both the phenotypes and genotypes of cells.[1,2] Conventional bulk cell assays, which operate under the assumption of cellular homogeneity, average out the properties of individual cells, thereby obscuring the variability and unique characteristics inherent within a cell population. This limitation has underscored the growing importance of single-cell level analysis in biological research, encompassing fields such as immunology,[3,4] cancer research,[5–7] and drug development.[8,9] Consequently, techniques in single-cell level analysis of genomics,[10–12] proteomics,[13–15] and metabolomics[16–18] have become pivotal in current research for the precise characterization of cellular states and functions, making single-cell analysis an essential tool for uncovering hidden genetic, cellular, and structural details. To achieve high-precision isolation and manipulation of individual cells for single-cell analysis, a myriad of techniques has been developed over the past decades. These methods include microwells,[19,20] micropatterns,[21,22] microtraps,[23,24] microvalves,[25,26] droplet-based techniques,[27,28] optical tweezers,[29,30] and magnetic tweezers,[31,32] and the use of dielectrophoretic forces[33,34] or optoelectronic tweezers.[35–38] However, they exhibit various limitations, including low throughput, buffer incompatibility, complex device fabrication, reduced biocompatibility due to additional labeling, and reliance on expensive, bulky external instruments. On the other hand, acoustic tweezers offer an alternative that is contact-free, biocompatible, and low-cost for manipulating individual cells, addressing some of these key challenges.

Acoustic tweezers, primarily utilizing surface acoustic waves (SAWs),[39–47] can effectively manipulate microparticles and cells

[a] Department of Mechanical and Aerospace Engineering, University of California at Los Angeles, USA. E-mail: peiyu@g.ucla.edu
[b] Department of Electrical and Computer Engineering, University of California at Los Angeles, USA
[c] Department of Chemical and Biomolecular Engineering, University of California at Los Angeles, USA
[d] Department of Microbiology, Immunology and Molecular Genetics, David Geffen School of Medicine, University of California at Los Angeles, USA
[e] Department of Bioengineering, University of California at Los Angeles, USA
[f] Institute for Quantitative and Computational Biosciences, University of California at Los Angeles, USA

† Electronic supplementary information (ESI) available. See DOI: https://doi.org/10.1039/d4lc00736k

by generating acoustic potential wells through standing acoustic waves. In SAWs, standing waves are generated by interdigitated transducers (IDTs), typically fabricated on a piezoelectric substrate such as lithium niobate ($LiNbO_3$). However, these devices are constrained by a limited active acoustic manipulation area due to the evanescent wave's decaying nature.[48] Recently, a novel acoustic device known as the compliant membrane acoustic platform (CMAP),[49–51] enabling near-field trapping of microparticles and cells over a large area. Unlike SAWs, CMAP does not rely on acoustic standing waves; instead, it utilizes large acoustic impedance mismatches to create a near-field acoustic potential gradient for patterning microparticles and cells at sub-wavelength resolution with complex, non-periodic acoustic potential profiles. However, CMAP cannot achieve single-cell level trapping and manipulation due to the difficulty of fabricating a thin and soft membrane structure over a narrow and high aspect ratio PDMS structure, only handling microparticles and cells in groups. Additionally, once microparticles and cells are trapped, CMAP lacks the capability to selectively release specific particles or cells for downstream collection and further analysis.

Herein, we present a novel acoustic microfluidic device designed for large scale single-cell trapping and selective releasing. Acoustic potential wells, generated by spherical air cavities within a PDMS substrate, provide the necessary acoustic radiation force for individual cell trapping and isolation. These potential minima are created as the acoustic wave travels through the patterned PDMS substrate. After trapping is complete, the near-infrared laser pulse can selectively disrupt the air cavities, releasing the microparticles or cells with the assistance of background flow. Our device not only allows large scale single cell trapping but also enables their deterministic

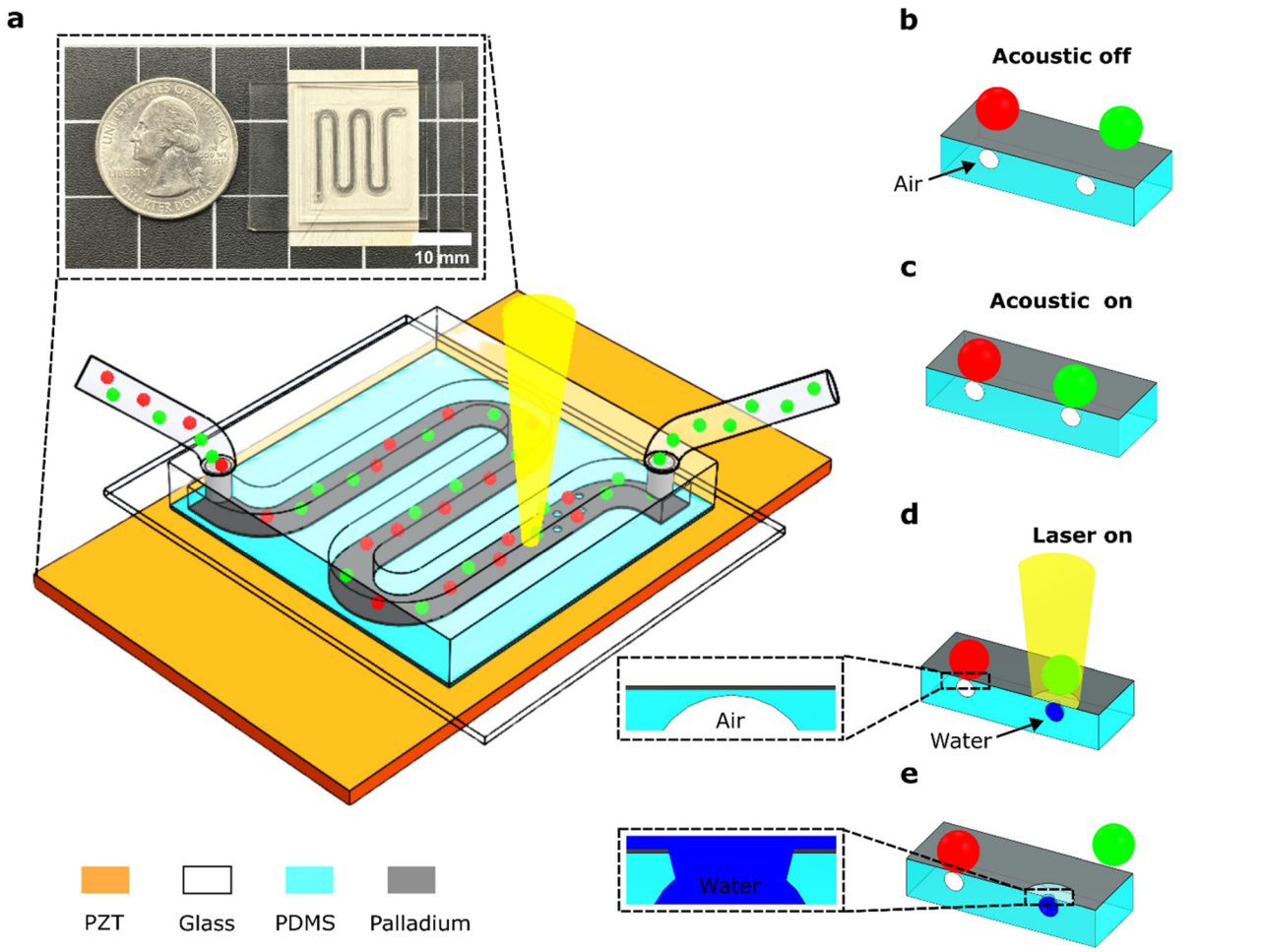

Fig. 1 (a) 3D diagram and schematic of the platform: the PZT substrate (orange), glass layer (transparent), PDMS structure embedded with spherical air cavities (light blue), thin palladium metal coating (dark gray), and the top PDMS microfluidic channel. The serpentine PDMS microfluidic channel (1 mm wide, 0.2 mm tall, and 10 cm long) allows for the trapping and selective release of particles and cells. The yellow beam represents the near-infrared laser used for the selective release process. (b–e) Cross-section view of the device to illustrates the working mechanism. (b) Acoustic off: microparticles and cells (represented by red and green spheres) remain randomly distributed and are not influenced by the air cavities. The air cavities, depicted as white circles, are located within the PDMS structure. (c) Acoustic on: microparticles and cells are trapped at the air cavities. (d) Laser on: laser is focused above the air cavities to selectively release the trapped particles. This process allows water to fill the air cavities. (e) Post-release: the trapped particles (green) are released and subsequently flushed downstream by the background flow. The red particles remain trapped due to the intact air cavities.

release. Additionally, the fabrication process is simple and requires no photolithography process, offering a low cost and rapid prototyping method for applications in single-cell analysis.

Results

Operation principle of the device

Fig. 1a presents the 3D diagram and schematic of the single cell CMAP device. It consists of a PZT substrate to provide acoustic excitation, a glass substrate with a PDMS structure embedded with spherical air cavities, a thin palladium metal coating to absorb near infrared irradiation, and a top serpentine-shaped PDMS microfluidic channel that serves both as a chamber and a fluid flow guide. Single-cell acoustic trapping is achieved by utilizing the air cavities next to the surface of a PDMS structure to create near-field acoustic potential wells generated by the significant acoustic impedance difference between air and the surrounding materials. PDMS is selected for its impedance properties, closely matching that of water, minimizing wave reflection and ensuring efficient acoustic energy transmission into the water layer.

The 3D spherically-shaped air cavities created by the microspheres form a tapered PDMS layer between the water and the air cavity, with the thinnest section at the center. This central region, being the softest and most compliant, keeps the lowest pressure area at the center of the air cavity during acoustic vibration. This creates a single precision trapping site at the center of each air cavity. This is advantageous compared to prior studies that utilize 2D air cavities formed by a planar PDMS membrane of the same thickness.[49–51] In those structures, microparticles tended to trap along the contour of these air cavities rather than at a single point.

Fig. 1b and c illustrate the process of acoustic trapping. After individual microparticles and cells are trapped above the air cavities, background flow is introduced into the channel to flush out non-trapped particles. Next, a 1030 nm near-infrared laser (Thorlabs QSL103A, 500 ps pulse duration) is used to selectively release the particles. The near-infrared wavelength is chosen to minimize cellular absorption and scattering, thereby reducing photothermal or photochemical effects on cells. When the laser is focused above the air cavities, the palladium layer absorbs the laser energy, causing disruption of the thin PDMS membrane underneath. Water then fills the broken air cavities, nullifying the acoustic traps to release the particles above, which are subsequently flushed downstream by the background flow. The permanently nullified traps avoid re-trapping of cells released in the upstream. The schematics of the selective release are shown in Fig. 1d and e.

In Fig. 1d, the red particle is trapped above the intact thin PDMS membrane. The green particle, however, is released by laser-induced PDMS membrane rupture, which allows water to enter the cavity and nullify the acoustic trapping. SEM images showing the structure difference of an intact air cavity and a laser-disrupted cavity are presented in ESI† Fig. S7. The 10 nm thin palladium layer coated on the PDMS surface is for absorbing the laser energy but not changing the compliant membrane nature of the PDMS structure. The localized nature of the laser beam ensures that only the targeted air cavities are disturbed, allowing for precise and selective release of individual particles.

Device fabrication

Fig. 2 illustrates the fabrication process flow for manufacturing the single-cell CMAP device. The process begins with drying a liquid solution containing 5 μm PMMA beads on a PVC substrate, followed by pouring a PDMS precursor. A glass substrate, which serves as a carrier, is then pressed onto the uncured PDMS. After curing, the glass and PDMS layers are released from the PVC substrate by immersing in acetone. During this process, the PMMA microspheres, which were embedded just beneath the PDMS surface, dissolve and subsequently create air cavities as the solvent evaporates through a residual PDMS membrane between the air–water interface. Following this, a 10 nm thin palladium layer is selectively sputter-coated onto the PDMS surface (Dep Sputter – Denton Desk II) with a deposition time of 15 seconds. Palladium is chosen for its wide availability in SEM sputter coating. Other metallic materials should also work. This deposition is guided by a plastic shadow mask cut with a CO_2 laser (Glowforge Inc. 40W 3D laser cutter). After the plastic shadow mask is lifted off, a desired shape is patterned on the PDMS surface. Finally, a PDMS channel, molded using a CO_2 laser-cut plastic mold, is O_2 plasma bonded onto the PDMS layer containing the air cavities to complete the device.

Numerical simulation

The spherical shape of the cavities ensures a single tangential contact point at the PDMS structure surface, creating a single acoustic potential well directly above each air cavity. To verify our design, a COMSOL acoustic–structure interaction model is implemented (ESI† Fig. S8). Fig. 3a illustrates a three-dimensional COMSOL simulation of a single air cavity, showing the radiation potential profile for 10 μm polystyrene microspheres in water. Fig. 3b reveals the cross-sectional view of the three-dimensional simulation depicted in Fig. 3a. It demonstrates a sharp gradient drop in radiation potential from the bulk PDMS area to the air cavity area, indicating a steep decrease in potential energy as the 10 μm polystyrene microsphere moves from the bulk PDMS region towards the center of the air cavity. The lowest point in the radiation potential is located at the center of the air cavity. This steep gradient drop confirms the effectiveness of the air cavity in creating strong acoustic radiation forces. The presence of a single, potential minimum indicates that the trapping position is highly localized to the center of each air cavity.

To study the minimum separation distance between two neighboring traps, we simulated air cavities with varying spacing. In Fig. 3c, two air cavities spaced 15 μm apart create

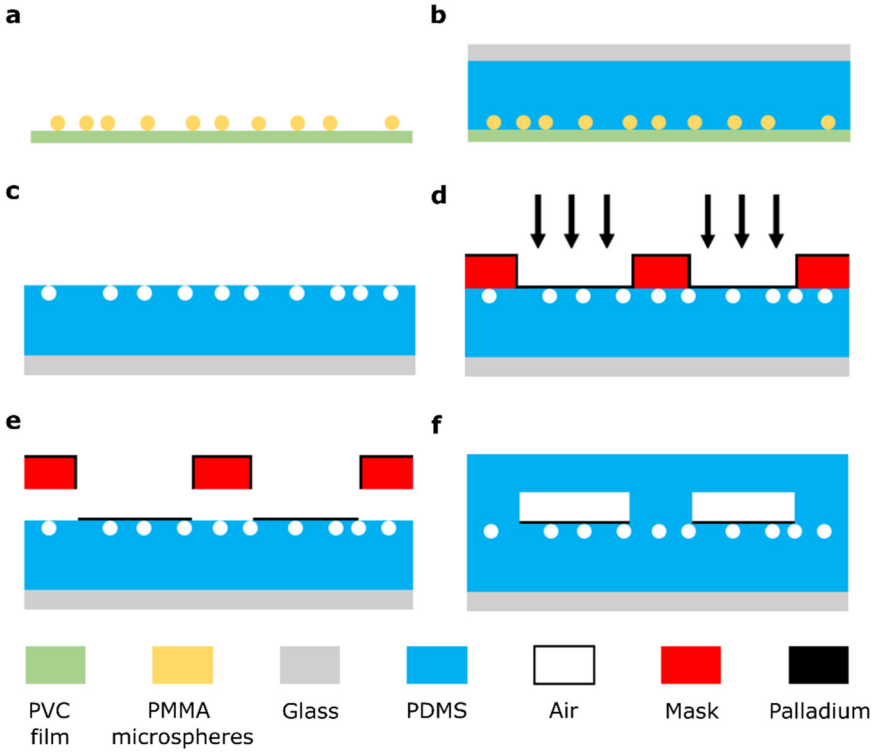

Fig. 2 (a) PMMA microspheres (5 μm) are deposited and dried on a PVC film substrate. (b) PDMS precursor is poured over the PMMA beads and pressed by a glass substrate to ensure uniformity. (c) After curing, the PDMS and glass are released from the PVC substrate by immersion in acetone, which dissolves the embedded PMMA microspheres, creating air cavities. (d) A thin palladium layer (10nm) is sputter-coated through a CO_2 laser-cut plastic shadow mask onto the PDMS surface. (e) The shadow mask is lifted off, leaving the palladium selectively deposited in the desired regions. (f) A PDMS microfluidic channel is O_2 plasma bonded with the PDMS layer containing the air cavities, completing the device fabrication.

distinct potential wells, which allow for separate single cell trapping at each cavity. However, as shown in Fig. 3d, when the spacing decreases to 10 μm, the potential wells merge, preventing individual trapping at each site. These simulation results predict that the minimum separation distance between two neighboring traps is around 10–15 μm.

To calculate the radiation force on microparticles, we calculate the spatial gradient of the potential energy distribution. For a particle of size much smaller than the wavelength ($D \ll \lambda$), the acoustic radiation force (ARF) can be approximated by the following expressions:[52]

$$\mathrm{ARF} = -\nabla U^{\mathrm{rad}} \tag{1}$$

$$U^{\mathrm{rad}} = \left(\frac{4\pi}{3}\right) a^3 \left\{ \left[1 - \left(\frac{\kappa_p}{\kappa_o}\right)\right] \frac{1}{2} \kappa_o \langle p^2 \rangle - \left[\frac{\left(2\left(\frac{\rho_p}{\rho_o} - 1\right)\right)}{\left(2\left(\frac{\rho_p}{\rho_o}\right) + 1\right)}\right] \left(\frac{3}{4}\right) \rho_o v^2 \right\} \tag{2}$$

where ARF represents the acoustic radiation force (ARF), U^{rad} is the acoustic potential energy, a denotes the particle radius, and p and v are the first-order acoustic pressure and velocity at the particle, respectively. The compressibility (κ) and density (ρ) are subscripted as 'p' for the particle and 'o' for the surrounding medium. The ARF is the negative gradient of the acoustic potential energy U^{rad}. This indicates that the ARF acts in the direction opposite to the gradient of the acoustic potential. Consequently, in our device, microparticles will be transported to the potential minimum region by the acoustic radiation forces (ARF) resulting from the non-uniform acoustic potential distribution. In addition, based on Fig. 3b and eqn (1), the gradient of the potential is steepest near the air cavity area, indicating that the ARF is strongest in this region. As the distance from the air cavity center increases, the potential gradient becomes smaller, indicating that the ARF decreases in magnitude.

Experimental trapping results of polystyrene microspheres

To characterize the forces applied on a single particle, we conducted single particle position tracking to obtain distance and velocity information. For the acoustic radiation force analyzed in our experiments, all the 10 μm polystyrene particles were suspended in DI water and were pulled into the potential wells by the acoustic radiation force. During this process, the induced Stokes drag force counteracts with this acoustic radiation force so that the acoustic radiation force can be determined by examining the velocity of the particles. The movements of 10 μm microparticles were recorded in individual videos with a frame rate of 1200 s^{-1} (Chronos 2.1-HD High

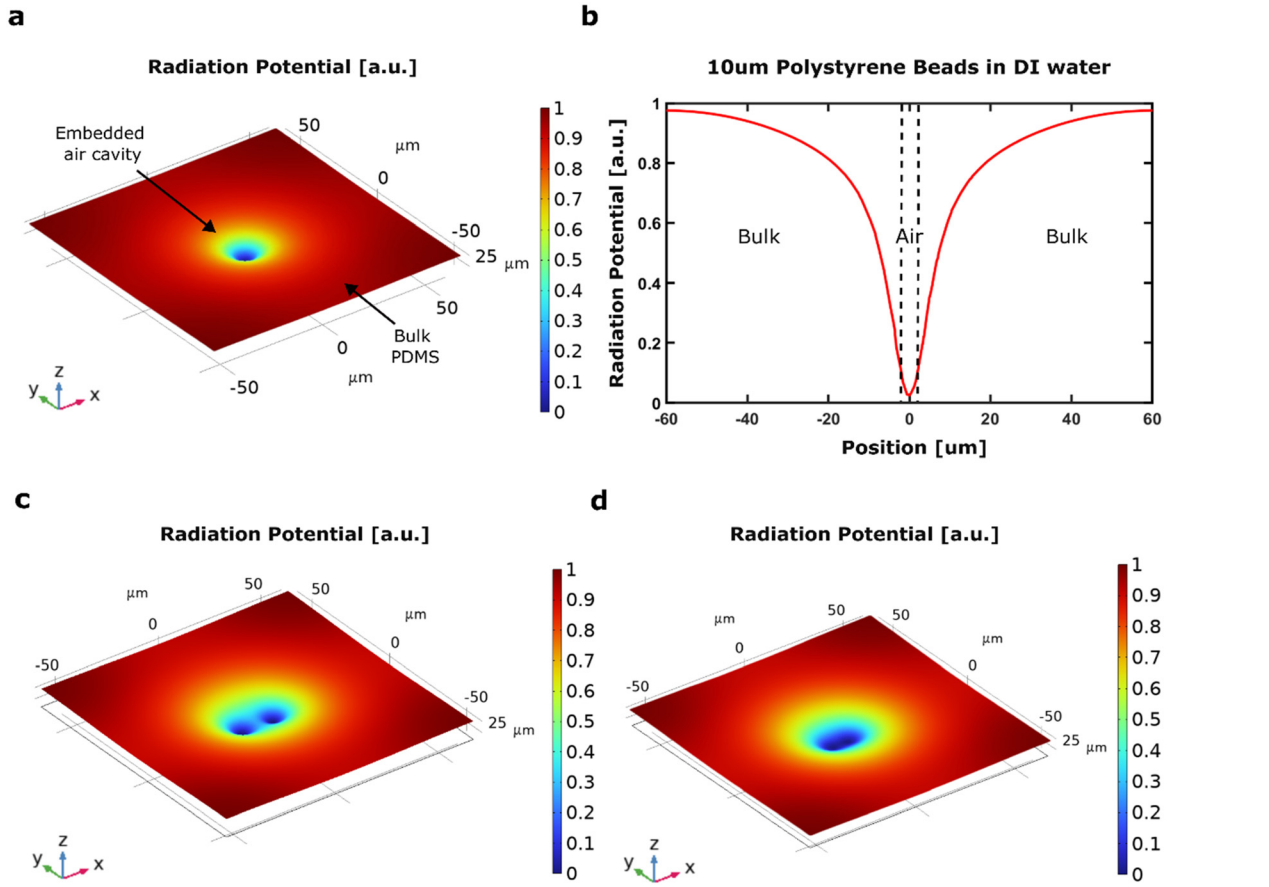

Fig. 3 (a) 3D COMSOL simulation of acoustic radiation potential generated by a single embedded air cavity within a 120 μm × 120 μm PDMS area, illustrating a strong localized potential well. (b) Cross-sectional profile of the radiation potential along the *x*-axis, highlighting a sharp gradient from bulk PDMS to the air cavity center. (c) Acoustic radiation potential distribution of two air cavities spaced 15 μm apart, showing distinct potential wells that enable individual trapping at each site. (d) When the cavity spacing is reduced to 10 μm, the potential wells merge, resulting in a single broader well that prevents isolated trapping at each cavity location.

Speed Camera). The displacement of each single particle can be determined using Trackmate software (ImageJ). Then, the particle velocity can be calculated by using the displacements and the time intervals between each frame. The Stokes drag force acting on a particle can be expressed as:

$$F_{\text{drag}} = 6\pi\eta r v \tag{3}$$

where η is the fluid viscosity, r is the radius of a single spherical particle, and v is the particle velocity. In our experiment, microspheres are located at the bottom surface in the microfluidic channel. The Stokes drag force increases as a particle approaches the wall of a channel due to the altered hydrodynamic interactions between the particle and the fluid caused by the nearby surface. Therefore, the Stokes drag force is corrected as follows:

$$F_{\text{drag}} = 6\pi\eta r v\chi \tag{4}$$

where χ is the correction factor for parallel translation along surfaces. According to Faxén's correction,[53,54] this factor can be expressed using a fifth-order power series expansion:

$$\chi = \frac{1}{1-\frac{9}{16}\left(\frac{r}{z}\right)+\frac{1}{8}\left(\frac{r}{z}\right)^3-\frac{45}{256}\left(\frac{r}{z}\right)^4-\frac{1}{16}\left(\frac{r}{z}\right)^5} \tag{5}$$

This adjustment is crucial for accurately calculating the drag force experienced by a particle near a flat surface, accounting for the modified hydrodynamic interactions. Since for our case, particles are located at the bottom, the $\frac{r}{z}$ ratio is 1. By plugging the ratio into eqn (5), the resulting Faxén's correction is around 3.083. By incorporating the velocity data and applying Faxén's correction into eqn (3) and (4), the drag force of the particle can be calculated. Fig. 4a shows the measured trapping force and the simulated acoustic radiation force (ARF) profiles for a single 10 μm polystyrene microsphere trapped by an air cavity. As the 10 μm microsphere moves toward the air cavity center, the simulated trapping force increases rapidly and returns to zero when fully trapped. The measured trapping force closely follows the trend predicted by the simulation, validating the accuracy of the computational model. The maximum ARF on the trapped particle is around 1289 pN, which is significantly larger than the background flow drag force. The background flow is maintained at 1.5 ml h^{-1} (KD Scientific Model 100 Syringe

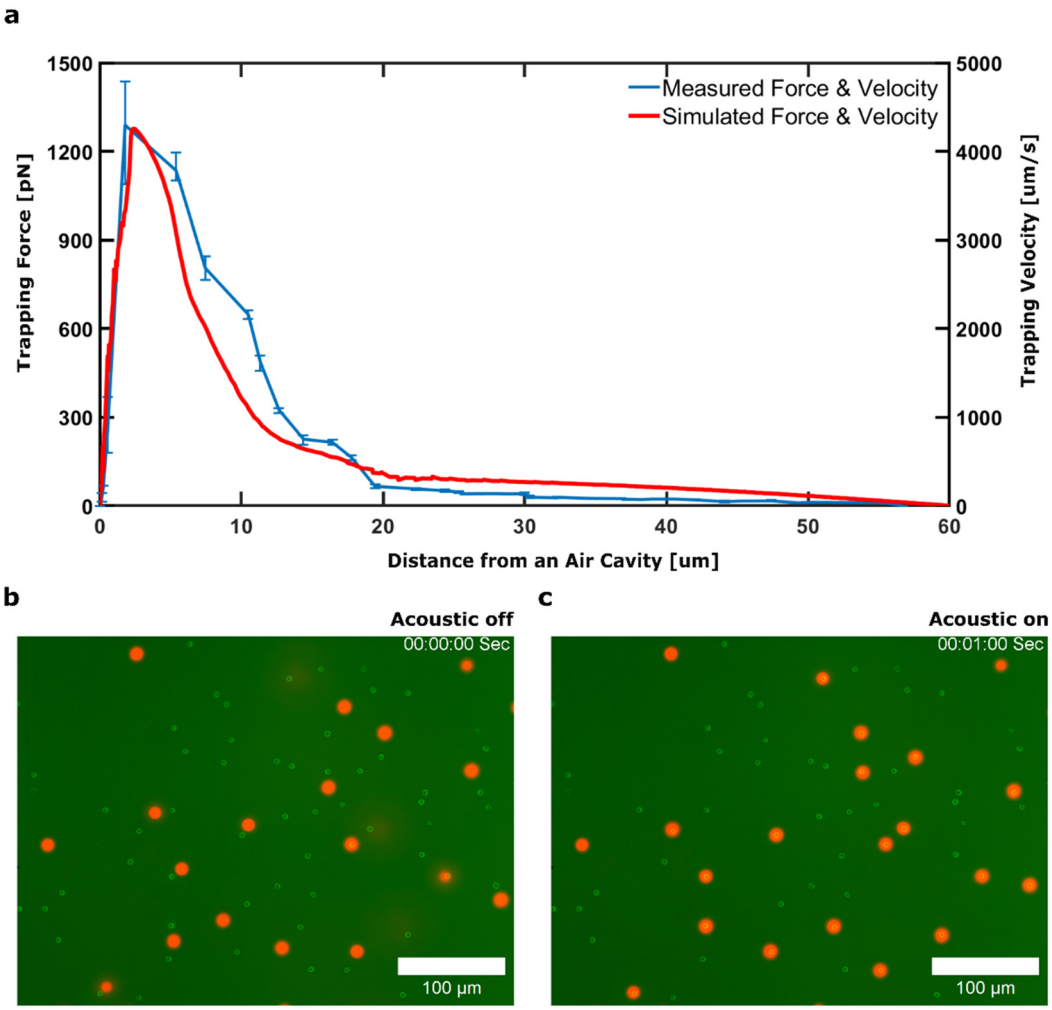

Fig. 4 (a) The experimental and numerically calculated trapping forces and velocities of a 10 μm polystyrene microsphere as a function of its distance from the center of an air cavity. The error bars represent the variation in measured trapping force across multiple trials. (b) Random distribution of 10 μm red fluorescent polystyrene microspheres on the device without acoustic field. (c) Trapping of 10 μm red fluorescent polystyrene microspheres at air cavities on the device with an applied acoustic field.

Infusion Pump) and based on the dimensions of the microfluidic channel (1 mm wide × 200 μm high × 10 cm long), the flow velocity is estimated to be approximately 304 μm s^{-1} at locations 5 μm above the channel surface. Calculations indicate that the drag force exerted by this flow is around 88 pN, which is significantly smaller than the acoustic radiation force (ARF). Consequently, when the acoustic field is activated, microparticles and cells will each be trapped at individual air cavity. The non-trapped redundant particles will be flushed away by the background flow, leaving only the trapped particles for selective release in the next step.

Fig. 4b and c demonstrate the microparticle trapping process. The PDMS is stained with BODIPY dye, resulting in green fluorescence for enhanced contrast and image quality. Fig. 4b depicts the distribution of 10 μm fluorescent polystyrene microspheres (red) on the device surface in the absence of an acoustic field. The microspheres are randomly distributed. Background features tiny green circles, representing the locations of the 5 μm air cavities, which are also randomly distributed. Maintaining an appropriate concentration of air cavities is crucial to avoid overlapping and ensure individual trapping. Upon activation of the acoustic field, the red microspheres migrate rapidly towards the nearby air cavities and become securely trapped as shown in Fig. 4c (see also the ESI† Video S1).

As shown in Fig. 4a, the effective trap range is approximately 10 μm from the center of a trap. This explains why, once a 10 μm bead occupies the trap, a second bead cannot be effectively captured. The same principle applies to single-cell trapping: the shape of the potential energy profile remains consistent, with the only difference being the peak velocity value. Consequently, when a single cell occupies a trap, any additional cells are unable to enter the strong trapping zone and are flushed away by the background flow.

Trapping results of biological samples

Biocompatibility of the acoustic devices is tested using A20 lymphoma, a type of suspension cell (see the Experimental

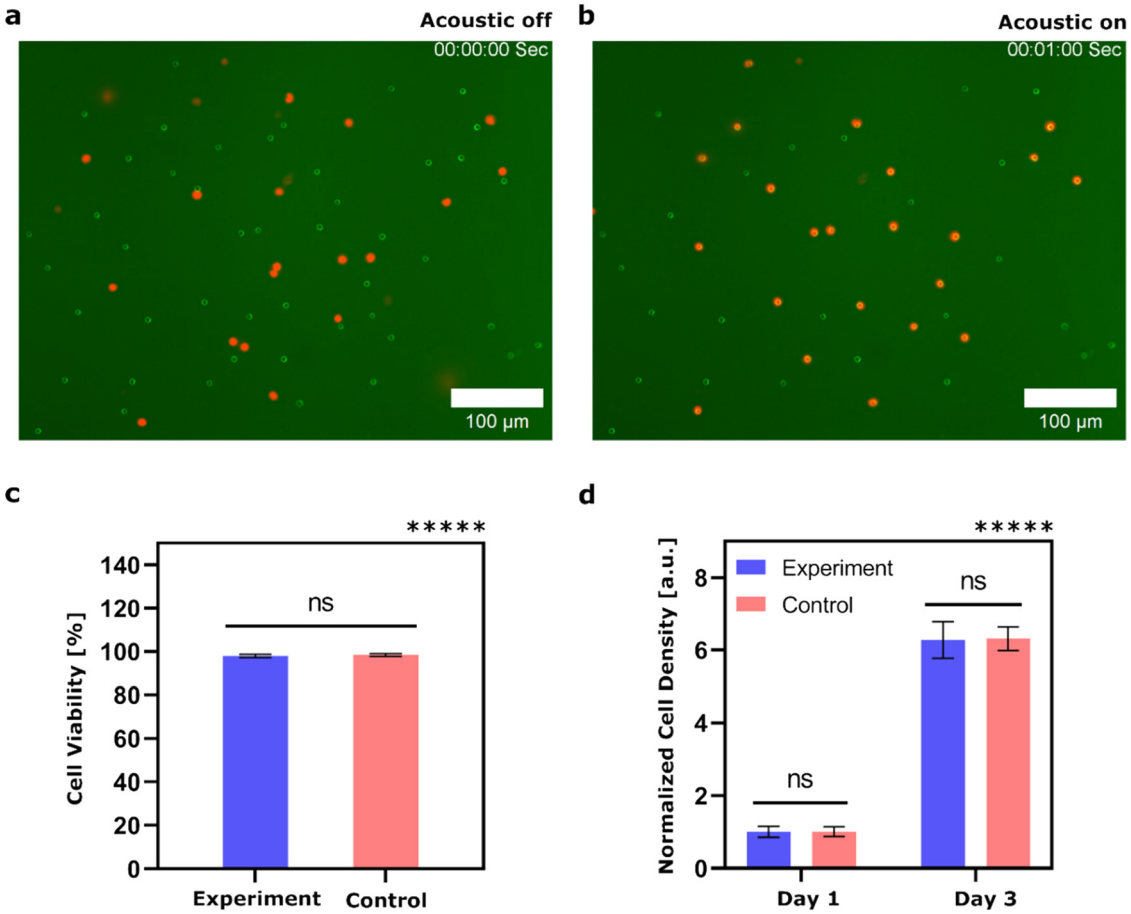

Fig. 5 (a) Random distribution of A20 lymphoma cells (red) on the device without acoustic field. (b) Acoustic trapping of A20 lymphoma cells (red) at air cavities on the device with an applied acoustic field. (c) Viability assessment of A20 lymphoma compared to the control. (d) Proliferation assessment of A20 lymphoma cells after 48 hours of incubation compared to the control. (*****number of trials measured, n = 5, ns: not significant).

section for details on cell culturing). A20 cells are stained with SYTO 59 red fluorescent dye for about 30 minutes before the experiment. As illustrated in Fig. 5a, without an acoustic field, these cells are randomly dispersed on the device surface. When the acoustic field is activated, as depicted in Fig. 5b, the red A20 cells migrate towards the nearest air cavities and become securely trapped. This trapping result of the cells resembles the results observed with polystyrene beads in Fig. 4c, demonstrating the device's capability to trap suspension cells efficiently with the acoustic field (ESI† Video S2).

LNCaP cells, a type of adherent cell (see the Experimental section for details on cell culturing), are also used to test the biocompatibility of our device. The green fluorescent color of LNCaP cells is generated by transducing LNCaP cells with a lentivirus carrying the GFP reporter gene, thus the PDMS is stained with Nile Red dye to provide a red background for better contrast. In Fig. 6a and b, the trapping process of LNCaP cells is depicted before and after the acoustic field is activated. Upon activation of the acoustic field, the cells migrate towards the air cavities and are trapped (ESI† Video S3).

Following the trapping of A20 and LNCaP cells in the device at 3 MHz and 17 V_{pp} for approximately 10 minutes, cell viability was assessed using trypan blue staining (ATCC) and quantified with a hemocytometer (Hausser Scientific Reichert Bright-Line), in accordance with the manufacturers' protocols. For the control group, cells were placed in the device without exposure to the acoustic field for the same duration as the experimental group. The viability of A20 cells in the experimental group was 97.92%, closely comparable to 98.36% in the control group (Fig. 5c). Similarly, LNCaP cells in the experimental group exhibited a viability of 94.87%, nearly identical to the control group's 95.39% (Fig. 6c). Statistical analysis using an unpaired t-test revealed no significant difference between the experimental and control groups ($p > 0.05$). To further evaluate biocompatibility, cell proliferation was assessed. Portions of both control and experimental cells were incubated for an additional 48 hours post-experiment (from day 1 to day 3). Cell densities were estimated and normalized at day 1 and day 3 using a hemocytometer. A20 cell densities increased sixfold (Fig. 5d), while LNCaP cell densities doubled (Fig. 6d), demonstrating the device's good biocompatibility. Unpaired t-tests comparing cell proliferation between experimental and control groups confirmed no statistically significant differences ($p > 0.05$), further supporting the device's compatibility with both cell viability and proliferation.

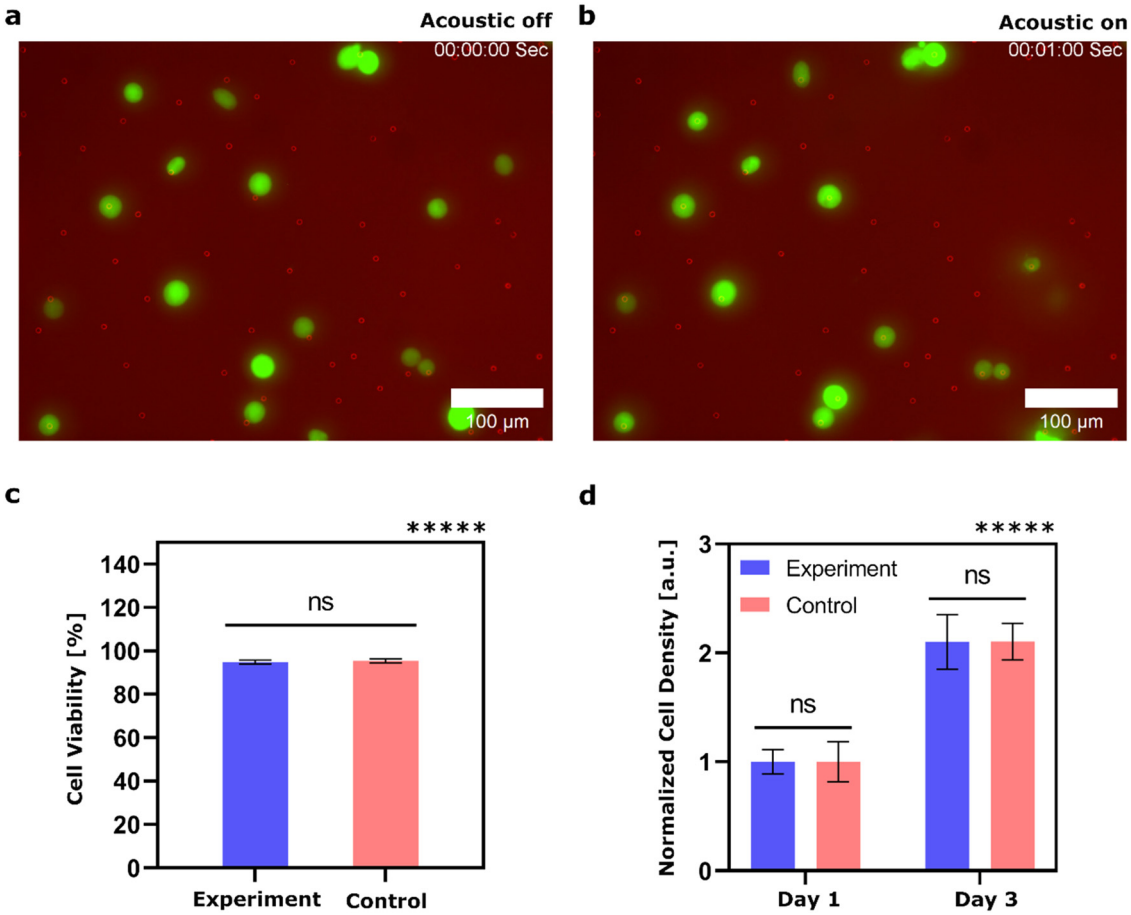

Fig. 6 (a) Random distribution of LNCaP cells (green) on the device without acoustic field. (b) Acoustic trapping of LNCaP cells (green) at air cavities on the device with an applied acoustic field. (c) Viability assessment of LNCaP cells compared to the control. (d) Proliferation assessment of LNCaP cells after 48 hours of incubation compared to the control (*****number of trials measured, n = 5, ns: not significant).

Selective releasing of polystyrene microspheres

Fig. 7 demonstrates the selective release process of fluorescent microspheres using a 1030 nm near-infrared picosecond laser (Thorlabs QSL103A). For the laser selective release process, the device is coated with a thin layer (10 nm) of palladium. In Fig. 7a, 10 µm red and green fluorescent polystyrene microspheres are trapped at individual air cavities while the background flow is on. Fig. 7b–d illustrate the sequential selective release process. Our device is mounted on motorized stages, positioning each microsphere sequentially under the fixed laser focus. The laser selectively breaks the air cavities, releasing green microspheres, which are then flushed downstream by the background flow, leaving only red microspheres trapped on the device (ESI† Video S4). The red microspheres remain trapped as their air cavities are still intact. The precision of this process is ensured by a shutter that opens for 40 ms when the laser is directly above the target green microsphere, preventing the accidental release of other microspheres. The white dashed circles indicate the original locations of the green microspheres after their release. This selective release mechanism demonstrates the device's capability to selectively release specific particles. Furthermore, this experiment also confirms our theoretical prediction regarding the minimum spacing between neighboring traps. As shown in the upper right corner of Fig. 7(c and d), our method can selectively release one of two neighboring particles separated by a distance of 11 µm.

Selective releasing of biological samples

To demonstrate selective single cell release, a mixture of live and dead A20 cells was prepared. Live cells were stained with Calcein AM fluorescent dye, and dead cells were stained with SYTOX Orange for 30 minutes before the experiment. After washing with PBS to remove excess dye, the cells were mixed in the culture medium. The live cells (green) were sequentially released using the same process as in the selective release of microspheres. The live cells (green) were collected downstream, while the dead cells (red) remained trapped (Fig. 8a–d) (ESI† Video S5).

To prevent potential thermal damage from the PZT, a thermoelectric cooler was placed under the device during operation (details in the Experimental section). Collected cells were maintained at 37 °C in a portable incubator (Darwin Chambers) to minimize temperature influence on cell viability.

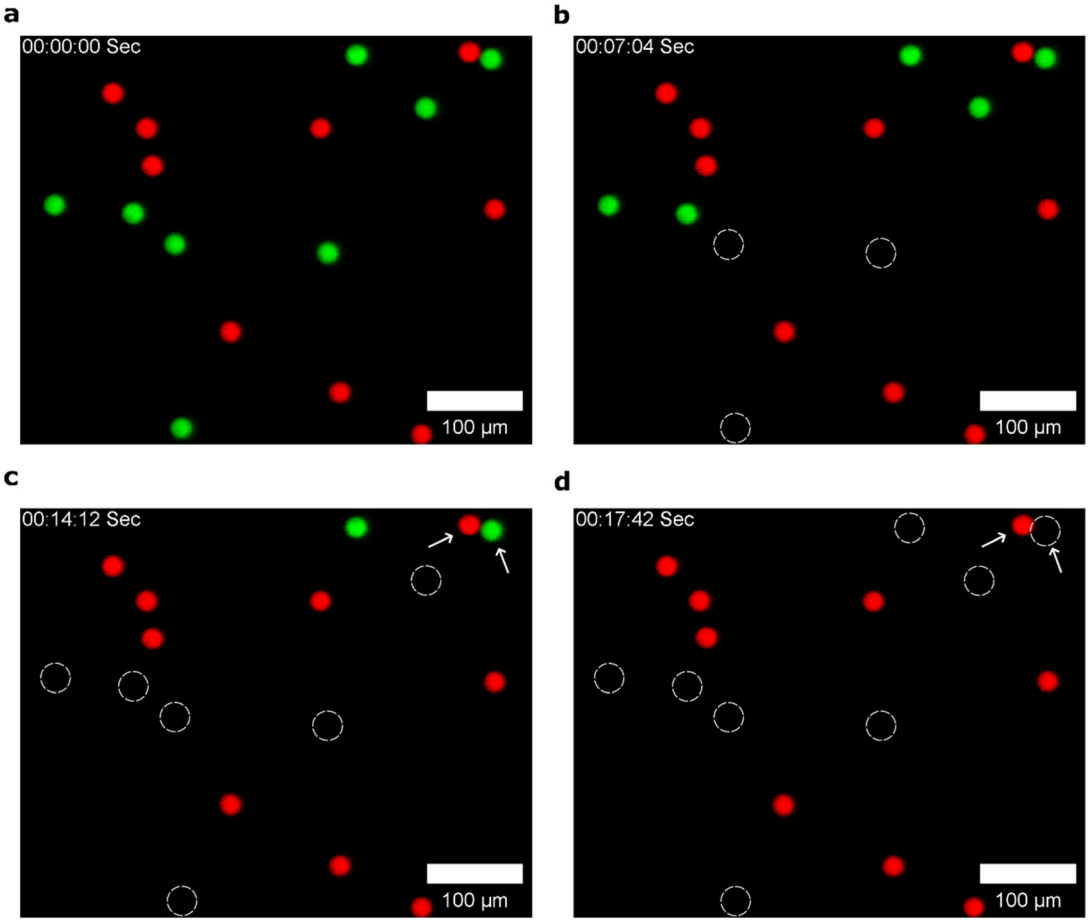

Fig. 7 (a) Initial distribution of green and red fluorescent microspheres trapped by air cavities with the acoustic field on. (b–d) Gradual and selective release of green fluorescent microspheres, leaving only red microspheres. The white dashed circles indicate the original locations of the released green microspheres.

The average selective release rate was approximately 40 cells per minute. Cell viability was assessed after collecting cells for 120 minutes. For the control group, cells were placed in the device without exposure to either the acoustic field or the laser and maintained for the same duration as the experimental group. The experimental sample exhibited a viability of 96.84%, closely comparable to the control group's 97.33% (Fig. 8e). An unpaired *t*-test indicated no significant difference between the experimental and control groups ($p > 0.05$). Cell proliferation was also assessed by incubating cells collected from both the control and experimental groups for 48 hours. The cell density increased by approximately fivefold from day 1 to day 3, like the control group, demonstrating good biocompatibility (Fig. 8f). The unpaired *t*-test showed no significant difference in proliferation between the experimental and control groups, confirming the device's suitability for biocompatible applications.

Discussion

This work introduces a novel acoustic microfluidic device designed for large-scale single cell trapping and selective releasing. This device utilizes spherical air cavities embedded in PDMS to create acoustic potential wells, effectively immobilizing both synthetic microparticles and biological cells. A near-infrared laser is integrated to enable selective release without compromising cell viability or proliferation, highlighting the device's suitability for downstream single-cell analysis applications. Additionally, our device is cost-effective and requires no photolithography process, allowing rapid prototyping.

The spherical shape effect of air cavity

The spherical shape of the bead is critical for controlling the trap's positioning. It forms a tapered PDMS film between the water and the air cavity, with the thinnest part located at the center. This softest, most compliant region ensures that the lowest pressure area remains at the center of the air cavity during acoustic vibration, enabling precise trapping position.

Although the active acoustic manipulation area demonstrated in this manuscript is 1 cm^2, the operational mechanism allows for extension of the manipulation area to tens or even hundreds of cm^2, enabling the trapping of more than a million single cells. This scalability can be achieved by

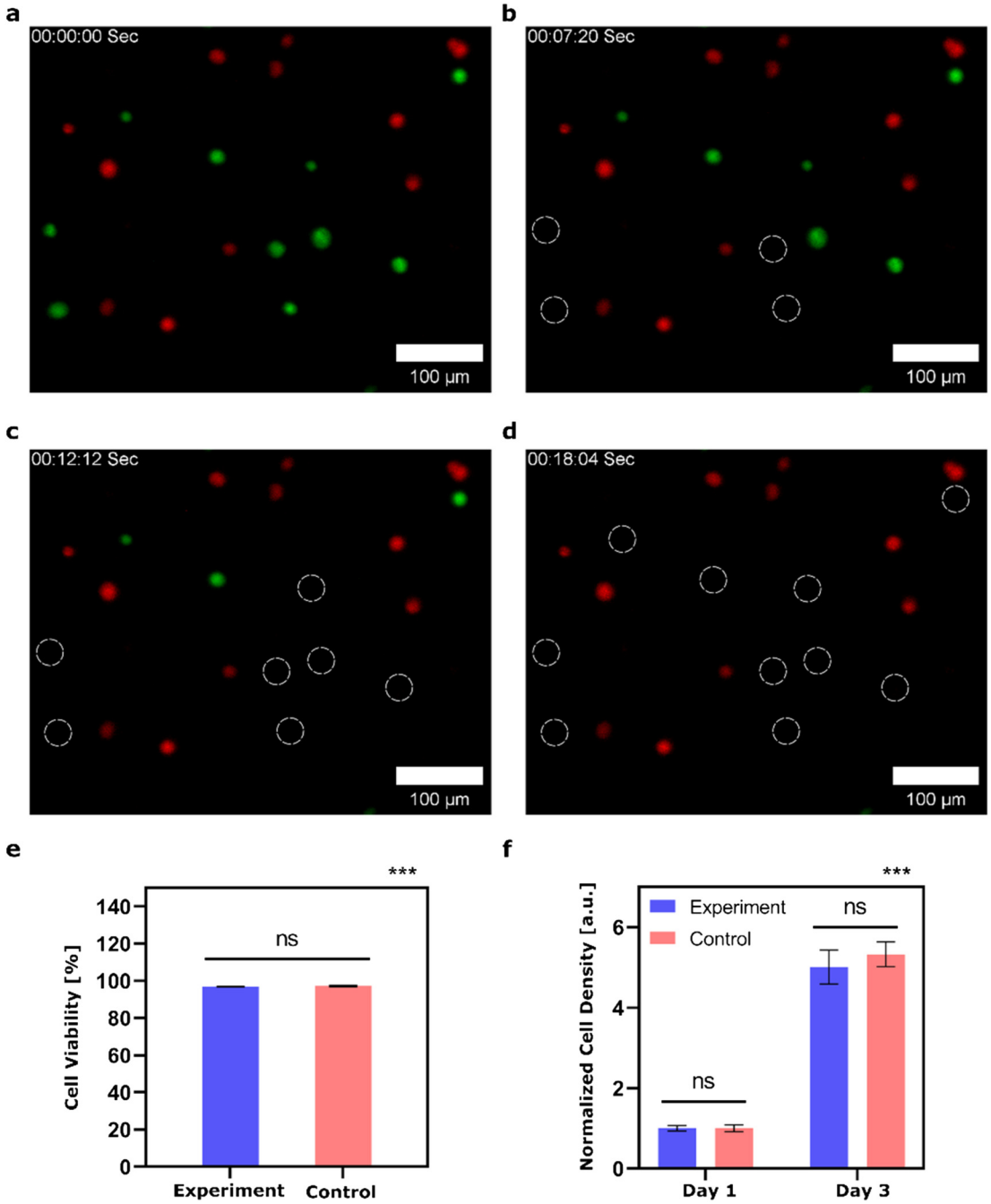

Fig. 8 (a–d) Gradual and selective release of live A20 cells (green), leaving only dead cells (red). The white dashed circles indicate the original locations of the released live cells (green). (e) Comparison of A20 cell viability between the experimental and control groups. (f) Comparison of A20 cell proliferation between the experimental and control groups on day 1 and day 3 (***number of trials measured, n = 3, ns: not significant).

parallelly connecting multiple PZT chips or by using a large-sized PZT substrate.

The potential acoustic microstreaming effect

Acoustic microstreaming is a widely used phenomenon for manipulating microscale objects through fluidic vortices generated near vibrating microstructures.[55–60] This effect is particularly prominent at low frequencies (<1 MHz). However, traps created by acoustic streaming are inherently unstable. To suppress acoustic streaming on our device, we operate at a higher frequency of 3 MHz.

We observed that at a vibration frequency of 500 kHz, significant acoustic streaming occurs near each trap, as demonstrated by the movement of 1 μm tracer beads (ESI† Video S6). In contrast, when the vibration frequency is increased to 3 MHz, the acoustic streaming effect is almost entirely suppressed.

Single cell trap efficiency and density

To evaluate the single cell trapping efficiency, 12 examination field- of-view areas along the entire fluid channel were randomly sampled. Successful single cell trapping is counted when there is only one cell on one acoustic trap. If a cell's position is not aligned with the acoustic trap position, potentially due to cell adhesion to the device surface, it is counted as a failed trap. If there are more than one cells trapped on the same acoustic trap, potentially due to cell clustering, it is also counted as a failed trap. Based on this definition, our device yields a single cell trapping efficiency of 94.09% with STD +/− 4.75%. (Fig. S9†)

This high trapping efficiency is achieved as long as the number of introduced cells is significantly lower than the total number of available traps. With the current fabrication method, 20 000 traps can be produced within a 1 cm^2 area (1 mm tall × 10 cm long serpentine channel). As shown in Fig. 5, approximately 50% of these traps are filled with single cells, corresponding to around 10 000 trapped cells on the device.

Imperfections in the fabrication process can reduce the number of functional air cavities. Based on an analysis of experimental data (Fig. S10†), the yield of functional air cavities is 90% of the total fabricated cavities. However, these fabrication imperfections do not affect the single-cell trapping efficiency as long as the number of functional air cavities significantly exceeds the target number of single cells to be trapped—typically at least 2× as many.

Permanently disabled traps and large area selective release

Furthermore, single cells trapped by air cavities are released through laser disruption of the cavity membranes. Once disrupted, a cavity does not reactivate for trapping. This feature avoids single cells released in the upstream to get re-trapped in the downstream after the laser beam is removed. This mechanism is crucial for achieving large-area single-cell trapping and selective release without increasing operational complexity compared to previous methods. For instance, in optical tweezers or optoelectronic tweezers (OET), projected light patterns must cover the active area to trap cells, limiting the active manipulation area or the number of cells that can be trapped in parallel. Typically, these active manipulation ranges are less than 100 μm for optical tweezers and 1 mm for OET.[35] In contrast, the mechanism demonstrated here provides 2–4 orders of magnitude increase of capacity for single cell trapping and releasing capability.

Future improvements

The current device can be further improved in two directions. One is the fabrication of well-organized air cavities and another is the automation of the single cell releasing process. In Fig. 4, 5, and 6, the air cavities are randomly distributed within the PDMS structure. Our current manufacturing method does not allow for the patterning of these air cavities in a periodic or orderly manner with even spacing. To ensure that each air cavity is distinct and adequately spaced from the others, we dilute the PMMA microspheres used to create these cavities to a low concentration. For our single cell trapping and selective release applications, the random distribution of air cavities does not affect the device's performance. However, in the future, developing a method to fabricate air cavities in a periodic order could further enhance the trapping density and throughput.

The second aspect that can be further improved is the automation process. In the current selective release setup, the scanning stage and solenoid shutter are manually controlled. While we achieve a selective release rate of approximately 40 cells per minute, automating the entire process would significantly enhance throughput and reduce labor cost.

Conclusion

We have developed a novel acoustic microfluidic device capable of large-scale single-cell trapping and selective release. This device uses spherical air cavities embedded in PDMS to create acoustic potential wells, enabling the individual trapping of both synthetic microparticles and biological cells across a 1 cm^2 area, accommodating a broad size range from 8 to 30 μm. The integration of a near-infrared laser facilitates selective release, achieving a release rate of approximately 40 cells per minute without compromising cell viability or proliferation. This demonstrated mechanism also holds potential for extending the manipulation area, enabling even larger-scale single-cell processing. A simple fabrication process, which does not require photolithography, supports the development of a low-cost and disposable device. Overall, our acoustic microfluidic system offers a robust, biocompatible, and cost-effective method for single-cell trapping and selective release, with significant potential for applications in genomics, proteomics, and other fields requiring precise single-cell analysis.

Experimental section

Laser setup

The current laser setup includes a 1030 nm near-infrared laser source (Thorlabs QSL103A), which emits a beam that passes sequentially through a solenoid electromagnet shutter, ND filters (Thorlabs mounted NIR Absorptive ND Filters), and a 10× objective lens (Nikon CFI Plan Fluor, 10×). The Thorlabs QSL103A laser operates with a pulse duration of 500 ps, a pulse energy of 40 μJ, and a repetition rate of 9 kHz. ND filters attenuate the pulse energy from 40 μJ to about 0.025 μJ, and the 10× objective lens focuses the beam diameter from 3 mm to approximately 15 μm. The solenoid shutter controls the laser beam by turning it on and off. The shutter speed is around 40 msec. A polarizing beam splitter cube (PBS 124, 1/2″, 1200–1600 nm) redirects a portion of the beam vertically downward to focus precisely on the platform located below. Our platform is mounted on two Thorlabs Z825B single axis stages, one for the *x*-axis and the other for

the *y*-axis, controlled by two Thorlabs TDC001 controllers. This configuration allows precise positioning of the target area under the focused laser beam, ensuring accurate control and delivery of the laser beam to the desired target area.

Acoustic device operation

The setup for operating the acoustic device is like that in our prior work.[46–48] It consists of a power amplifier (ENI Model 2100 L), a function generator (Agilent Model 33220A), a T.E. cooler (T.E. Technology Model CP-031HT), an ultra-long working distance microscope lens (20× Mitutoyo Plan Apo), an upright microscope (Zeiss Model Axioskop 2 FS), and a mounted recording camera. In our experiment, three kinds of cameras were used, (Zeiss Model AxioCam mRm), (IDS camera UI-3080CP-M-GL), and (Chronos 2.1-HD High Speed Camera). The function generator sends A.C. signals to the signal amplifier, which is electrically connected to the PZT substrate. The PZT will then convert the electrical signals into mechanical waves, which vibrates the substrate and creates acoustic traveling waves that propagate through the platform. To prevent potential thermal damage generated by PZT, a T. E. cooler is placed under the device while operating. The device is positioned under the Mitutoyo lens mounted on the Zeiss microscope.

Device fabrication

A 25 μm thick PVC thin film is treated with oxygen plasma for 1 minute to render the surface hydrophilic, facilitating the spreading of a liquid solution containing 5 μm PMMA microspheres. The PMMA solution, originally purchased from Lab 261 and diluted to 1 million per ml, is deposited onto the PVC film and allowed to dry in a vacuum chamber for 8 hours, resulting in a random distribution of microspheres on the film surface. Uncured PDMS is then poured over the PVC film, covering the PMMA microspheres, and a 1 mm thick cover glass is placed on top to create a sandwich structure with the PVC film at the bottom, PMMA microspheres embedded in PDMS in the middle, and the glass cover on top. The PDMS is prepared using 220 wt% Sylgard PDMS 527A, 220 wt% Sylgard PDMS 527B, 100 wt% Sylgard PDMS 184A, and 10 wt% Sylgard PDMS 184B (Curing Agent), based on 1 g of Sylgard PDMS 184A. The structure is subjected to vacuum to remove bubbles from the PDMS, and a weight is placed on top to ensure even stamping. The entire structure is baked at 60°C for 4 hours to cure the PDMS. After the PDMS solidifies, the structure is immersed in acetone, which dissolves both the PVC film and the PMMA microspheres, leaving behind spherical air cavities within the PDMS. A serpentine-shaped plastic mask is fabricated using a CO_2 laser cutter, and the PDMS with embedded air cavities is placed in a sputtering machine for 15 s (Dep Sputter – Denton Desk II). Using the mask, around 10 nm thick serpentine-shaped palladium layer is sputtered onto the structure. A serpentine-shaped PDMS microfluidic channel (1 mm wide, 200 μm high, 10 cm long) is fabricated using a mold. This microfluidic channel is then oxygen plasma bonded to the bottom PDMS structure containing the air cavities and palladium layer, completing the device assembly.

Numerical simulation

We used the acoustic–structural interaction module in COMSOL Multiphysics 6.1 with a finite element approach to simulate the acoustic radiation potential within the device chamber. Fig. S8† shows a cross-sectional view of the 3D model geometry used for simulation, which consists of a top fluid layer (water) and a bottom solid layer (PDMS). The central sphere represents an empty space corresponding to the air cavity within the PDMS layer. To simulate the vibration mode of the PZT element along its thickness, a prescribed displacement in the *y*-direction is applied at the bottom boundaries of the solid. An isotropic loss factor of 0.2 is included in the model to account for structural damping in PDMS. The finite element (FE) solver calculates the resulting total acoustic pressure in the fluid. This involves solving the acoustic–structure interaction at the fluid–solid interface, along with the inviscid momentum conservation equation (Euler's equation) and the mass conservation equation (continuity equation) within the fluid. Plane wave radiation was set around the top fluid boundaries to allow outgoing waves to leave the domain with minimal reflections (see also ESI† Fig. S8).

Polystyrene and PMMA beads

10 μm polystyrene green fluorescent beads are obtained from Thermo Fisher Scientific, USA. 10 μm polystyrene red fluorescent beads are obtained from Thermo Fisher Scientific, USA. 5 μm plain PMMA microspheres are obtained from Lab 261, USA.

Cell culturing

Materials. RPMI 1640 medium and fetal bovine serum (FBS) were purchased from Corning (Corning, NY). Penicillin–streptomycin (PS) was purchased from Thermo Fisher Scientific (West Hills, CA).

Methods. The A20 cell line was purchased from the American Type Culture Collection (ATCC, Rockville, MD) and cultured in Roswell Park Memorial Institute 1640 Medium (RPMI 1640), supplemented with 10% (vol/vol) fetal bovine serum (FBS, ThermoFisher Scientific) and 1% penicillin/streptomycin (Mediatech). A20 cells are cultured in T25 Nunclon Sphera flasks (ThermoFisher Scientific) at a concentration of 5×10^5 cells per mL in an incubator at 37°C and 5% CO_2. The medium is changed every two days and cells are transferred into 6-well plates at a concentration of 5×10^5 cells per mL and used for experiments.

The LNCaP cell line was purchased from the American Type Culture Collection (ATCC, Rockville, MD) and cultured in Roswell Park Memorial Institute 1640 Medium (RPMI 1640), supplemented with 10% (vol/vol) fetal bovine serum (FBS, ThermoFisher Scientific) and 1% penicillin/streptomycin

(Mediatech). GFP-LNCaP cells were generated by transducing LNCaP cells with a lentivirus carrying the GFP reporter gene. GFP-LNCaP cells are cultured in T75 Fisherbrand Tissue Culture flasks (Fisher Scientific) at a concentration of 3×10^5 cells per mL in an incubator at 37 °C and 5% CO_2. The medium is changed every two days and cells are resuspended and diluted at a concentration of 5×10^5 cells per mL and used for experiments.

All experiments were performed in compliance with policies and guidance provided by the UCLA Institutional Biosafety Committee (IBC), which is responsible for oversight of all research activities – including teaching laboratories – involving the use of hazardous biological material and recombinant or synthetic nucleic acids, as required and outlined in the NIH guidelines for research involving recombinant or synthetic nucleic acid molecules (NIH Guidelines) and the CDC/NIH Biosafety in Microbiological and Biomedical Laboratories (BMBL). All the experiments were approved by the UCLA Institutional Biosafety Committee (IBC) and no experimentation with human subjects was performed.

Data availability

The authors confirm that the data supporting the findings of this study are available within the article and its ESI.†

Author contributions

X. Z. is the main contributor who designed and fabricated the device, built the experimental setup, conducted the experiments, analyzed the data, and wrote the manuscript. X. Z. J. S. advised on the design of the laser setup and device fabrication process. A. Z., J. D., Y.-J. L. and A. G. assisted in conducting the simulations and fabricating devices. S. C., T. Q., and C.-H. L. prepared the A20 and LNCaP cells for the experiments, as well as shared their knowledge in cell culturing. J. W., Y. L., and N. L. advised on the cell experiments and provided equipment. P.-Y. C. supervised the project and revised the manuscript.

Conflicts of interest

There are no conflicts to declare.

Acknowledgements

This research is supported by the National Science Foundation NSF CMMI 2029454, NSF DBI 2345571, and the National Institute of General Medical Sciences (NIGMS) of the National Institutes of Health NIH R01GM127985.

References

1 J. P. Junker and A. van Oudenaarden, Every cell is special: genome-wide studies add a new dimension to single-cell biology, *Cell*, 2014, **157**(1), 8–11.
2 F. Buettner, K. N. Natarajan, F. P. Casale, V. Proserpio, A. Scialdone and F. J. Theis, *et al.*, Computational analysis of cell-to-cell heterogeneity in single-cell RNA-sequencing data reveals hidden subpopulations of cells, *Nat. Biotechnol.*, 2015, **33**(2), 155–160.
3 L. Zhang and Z. Zhang, Recharacterizing tumor-infiltrating lymphocytes by single-cell RNA sequencing, *Cancer Immunol. Res.*, 2019, **7**(7), 1040–1046.
4 J. Herderschee, C. Fenwick, G. Pantaleo, T. Roger and T. Calandra, Emerging single-cell technologies in immunology, *J. Leukoc. Biol.*, 2015, **98**(1), 23–32.
5 X. Zhang, S. L. Marjani, Z. Hu, S. M. Weissman, X. Pan and S. Wu, Single-cell sequencing for precise cancer research: progress and prospects, *Cancer Res.*, 2016, **76**(6), 1305–1312.
6 Y. Lei, R. Tang, J. Xu, W. Wang, B. Zhang and J. Liu, *et al.*, Applications of single-cell sequencing in cancer research: progress and perspectives, *J. Hematol. Oncol.*, 2021, **14**(1), 91.
7 B. Sun, Z. Xun, N. Zhang, K. Liu, X. Chen and H. Zhao, Single-cell RNA sequencing in cancer research: discovering novel biomarkers and therapeutic targets for immune checkpoint blockade, *Cancer Cell Int.*, 2023, **23**(1), 313.
8 B. Van de Sande, J. S. Lee, E. Mutasa-Gottgens, B. Naughton, W. Bacon and J. Manning, *et al.*, Applications of single-cell RNA sequencing in drug discovery and development, *Nat. Rev. Drug Discovery*, 2023, **22**(6), 496–520.
9 S. Mitra-Kaushik, A. Mehta-Damani, J. J. Stewart, C. Green, V. Litwin and C. Gonneau, The evolution of single-cell analysis and utility in drug development, *AAPS J.*, 2021, **23**(5), 98.
10 A. Tanay and A. Regev, Scaling single-cell genomics from phenomenology to mechanism, *Nature*, 2017, **541**(7637), 331–338.
11 I. C. Macaulay and T. Voet, Single cell genomics: advances and future perspectives, *PLoS Genet.*, 2014, **10**(1), e1004126.
12 I. C. Macaulay, W. Haerty, P. Kumar, Y. I. Li, T. X. Hu and M. J. Teng, *et al.*, G&T-seq: parallel sequencing of single-cell genomes and transcriptomes, *Nat. Methods*, 2015, **12**(6), 519–522.
13 J. Straubhaar, A. D'Souza, Z. Niziolek and B. Budnik, Single cell proteomics analysis of drug response shows its potential as a drug discovery platform, *Mol. Omics*, 2024, **20**(1), 6–18.
14 Y. Wang, Z. Y. Guan, S. W. Shi, Y. R. Jiang, J. Zhang and Y. Yang, *et al.*, Pick-up single-cell proteomic analysis for quantifying up to 3000 proteins in a Mammalian cell, *Nat. Commun.*, 2024, **15**(1), 1279.
15 J. Woo, S. M. Williams, L. M. Markillie, S. Feng, C. F. Tsai and V. Aguilera-Vazquez, *et al.*, High-throughput and high-efficiency sample preparation for single-cell proteomics using a nested nanowell chip, *Nat. Commun.*, 2021, **12**(1), 6246.
16 T. Hu, M. Allam, S. Cai, W. Henderson, B. Yueh and A. Garipcan, *et al.*, Single-cell spatial metabolomics with cell-type specific protein profiling for tissue systems biology, *Nat. Commun.*, 2023, **14**(1), 8260.
17 R. Zenobi, Single-cell metabolomics: analytical and biological perspectives, *Science*, 2013, **342**(6163), 1243259.

18 C. Seydel, Single-cell metabolomics hits its stride, *Nat. Methods*, 2021, **18**(12), 1452–1456.
19 J. Yuan and P. A. Sims, An automated microwell platform for large-scale single cell RNA-seq, *Sci. Rep.*, 2016, **6**(1), 33883.
20 L. Huang, Y. Chen, Y. Chen and H. Wu, Centrifugation-assisted single-cell trapping in a truncated cone-shaped microwell array chip for the real-time observation of cellular apoptosis, *Anal. Chem.*, 2015, **87**(24), 12169–12176.
21 D. Shin, J. You, A. Rahimian, T. Vu, C. Siltanen and A. Ehsanipour, *et al.*, Photodegradable hydrogels for capture, detection, and release of live cells, *Angew. Chem.*, 2014, **126**(31), 8360–8363.
22 C. S. Chen, M. Mrksich, S. Huang, G. M. Whitesides and D. E. Ingber, Geometric control of cell life and death, *Science*, 1997, **276**(5317), 1425–1428.
23 D. Di Carlo, L. Y. Wu and L. P. Lee, Dynamic single cell culture array, *Lab Chip*, 2006, **6**(11), 1445–1449.
24 A. M. Skelley, O. Kirak, H. Suh, R. Jaenisch and J. Voldman, Microfluidic control of cell pairing and fusion, *Nat. Methods*, 2009, **6**(2), 147–152.
25 M. A. Unger, H. P. Chou, T. Thorsen, A. Scherer and S. R. Quake, Monolithic microfabricated valves and pumps by multilayer soft lithography, *Science*, 2000, **288**(5463), 113–116.
26 H. S. Kim, T. P. Devarenne and A. Han, A high-throughput microfluidic single-cell screening platform capable of selective cell extraction, *Lab Chip*, 2015, **15**(11), 2467–2475.
27 F. Lan, B. Demaree, N. Ahmed and A. R. Abate, Single-cell genome sequencing at ultra-high-throughput with microfluidic droplet barcoding, *Nat. Biotechnol.*, 2017, **35**(7), 640–646.
28 L. Liu, C. K. Dalal, B. M. Heineike and A. R. Abate, High throughput gene expression profiling of yeast colonies with microgel-culture Drop-seq, *Lab Chip*, 2019, **19**(10), 1838–1849.
29 A. Keloth, O. Anderson, D. Risbridger and L. Paterson, Single cell isolation using optical tweezers, *Micromachines*, 2018, **9**(9), 434.
30 J. R. Kovac and J. Voldman, Intuitive, image-based cell sorting using optofluidic cell sorting, *Anal. Chem.*, 2007, **79**(24), 9321–9330.
31 W. Liu, N. Dechev, I. G. Foulds, R. Burke, A. Parameswaran and E. J. Park, A novel permalloy based magnetic single cell micro array, *Lab Chip*, 2009, **9**(16), 2381–2390.
32 R. Khojah, Z. Xiao, M. K. Panduranga, M. Bogumil, Y. Wang and M. Goiriena-Goikoetxea, *et al.*, Single-domain multiferroic array-addressable terfenol-d (smart) micromagnets for programmable single-cell capture and release, *Adv. Mater.*, 2021, **33**(20), 2006651.
33 B. M. Taff and J. Voldman, A scalable addressable positive-dielectrophoretic cell-sorting array, *Anal. Chem.*, 2005, **77**(24), 7976–7983.
34 Y. Qin, L. Wu, T. Schneider, G. S. Yen, J. Wang and S. Xu, *et al.*, A self-digitization dielectrophoretic (SD-DEP) chip for high-efficiency single-cell capture, on-demand compartmentalization, and downstream nucleic acid analysis, *Angew. Chem.*, 2018, **130**(35), 11548–11553.
35 P. Y. Chiou, A. T. Ohta and M. C. Wu, Massively parallel manipulation of single cells and microparticles using optical images, *Nature*, 2005, **436**(7049), 370–372.
36 Y. Yang, Y. Mao, K. S. Shin, C. O. Chui and P. Y. Chiou, Self-locking optoelectronic tweezers for single-cell and microparticle manipulation across a large area in high conductivity media, *Sci. Rep.*, 2016, **6**(1), 22630.
37 H. Y. Hsu, A. T. Ohta, P. Y. Chiou, A. Jamshidi, S. L. Neale and M. C. Wu, Phototransistor-based optoelectronic tweezers for dynamic cell manipulation in cell culture media, *Lab Chip*, 2010, **10**(2), 165–172.
38 K. W. Huang, T. W. Su, A. Ozcan and P. Y. Chiou, Optoelectronic tweezers integrated with lensfree holographic microscopy for wide-field interactive cell and particle manipulation on a chip, *Lab Chip*, 2013, **13**(12), 2278–2284.
39 S. C. S. Lin, X. Mao and T. J. Huang, Surface acoustic wave (SAW) acoustophoresis: now and beyond, *Lab Chip*, 2012, **12**(16), 2766–2770.
40 J. Shi, D. Ahmed, X. Mao, S. C. S. Lin, A. Lawit and T. J. Huang, Acoustic tweezers: patterning cells and microparticles using standing surface acoustic waves (SSAW), *Lab Chip*, 2009, **9**(20), 2890–2895.
41 D. J. Collins, B. Morahan, J. Garcia-Bustos, C. Doerig, M. Plebanski and A. Neild, Two-dimensional single-cell patterning with one cell per well driven by surface acoustic waves, *Nat. Commun.*, 2015, **6**(1), 8686.
42 X. Ding, S. C. S. Lin, M. I. Lapsley, S. Li, X. Guo and C. Y. Chan, *et al.*, Standing surface acoustic wave (SSAW) based multichannel cell sorting, *Lab Chip*, 2012, **12**(21), 4228–4231.
43 F. Guo, P. Li, J. B. French, Z. Mao, H. Zhao and S. Li, *et al.*, Controlling cell–cell interactions using surface acoustic waves, *Proc. Natl. Acad. Sci. U. S. A.*, 2015, **112**(1), 43–48.
44 S. Yang, Z. Tian, Z. Wang, J. Rufo, P. Li and J. Mai, *et al.*, Harmonic acoustics for dynamic and selective particle manipulation, *Nat. Mater.*, 2022, **21**(5), 540–546.
45 A. Ozcelik, J. Rufo, F. Guo, Y. Gu, P. Li and J. Lata, *et al.*, Acoustic tweezers for the life sciences, *Nat. Methods*, 2018, **15**(12), 1021–1028.
46 X. Ding, S. C. S. Lin, M. I. Lapsley, S. Li, X. Guo and C. Y. Chan, *et al.*, Standing surface acoustic wave (SSAW) based multichannel cell sorting, *Lab Chip*, 2012, **12**(21), 4228–4231.
47 D. J. Collins, C. Devendran, Z. Ma, J. W. Ng, A. Neild and Y. Ai, Acoustic tweezers via sub–time-of-flight regime surface acoustic waves, *Sci. Adv.*, 2016, **2**(7), e1600089.
48 O. Tigli and M. E. Zaghloul, Surface acoustic wave (SAW) biosensors, in *2010 53rd IEEE International Midwest Symposium on Circuits and Systems*, IEEE, 2010, pp. 77–80.
49 K. W. Tung, P. S. Chung, C. Wu, T. Man, S. Tiwari and B. Wu, *et al.*, Deep, sub-wavelength acoustic patterning of complex and non-periodic shapes on soft membranes supported by air cavities, *Lab Chip*, 2019, **19**(21), 3714–3725.
50 K. W. Tung and P. Y. Chiou, Field-programmable acoustic array for patterning micro-objects, *Appl. Phys. Lett.*, 2020, **116**(15), 151901.

51 X. Zhang, R. Son, Y. J. Lin, A. Gill, S. Chen and T. Qi, *et al.*, Rapid prototyping of functional acoustic devices using laser manufacturing, *Lab Chip*, 2022, **22**(22), 4327–4334.
52 H. Bruus, Acoustofluidics 7: The acoustic radiation force on small particles, *Lab Chip*, 2012, **12**(6), 1014–1021.
53 B. Lin, J. Yu and S. A. Rice, Direct measurements of constrained Brownian motion of an isolated sphere between two walls, *Phys. Rev. E*, 2000, **62**(3), 3909.
54 J. Leach, H. Mushfique, S. Keen, R. Di Leonardo, G. Ruocco and J. M. Cooper, *et al.*, Comparison of Faxén's correction for a microsphere translating or rotating near a surface, *Phys. Rev. E:Stat. Phys., Plasmas, Fluids, Relat. Interdiscip. Top.*, 2009, **79**(2), 026301.
55 M. Wiklund, R. Green and M. Ohlin, Acoustofluidics 14: Applications of acoustic streaming in microfluidic devices, *Lab Chip*, 2012, **12**(14), 2438–2451.
56 N. Nama, P. H. Huang, T. J. Huang and F. Costanzo, Investigation of acoustic streaming patterns around oscillating sharp edges, *Lab Chip*, 2014, **14**(15), 2824–2836.
57 P. Marmottant and S. Hilgenfeldt, Controlled vesicle deformation and lysis by single oscillating bubbles, *Nature*, 2003, **423**(6936), 153–156.
58 M. V. Patel, I. A. Nanayakkara, M. G. Simon and A. P. Lee, Cavity-induced microstreaming for simultaneous on-chip pumping and size-based separation of cells and particles, *Lab Chip*, 2014, **14**(19), 3860–3872.
59 Y. Okabe, Y. Chen, R. Purohit, R. M. Corn and A. P. Lee, Piezoelectrically driven vertical cavity acoustic transducers for the convective transport and rapid detection of DNA and protein binding to DNA microarrays with SPR imaging—A parametric study, *Biosens. Bioelectron.*, 2012, **35**(1), 37–43.
60 Y. Lin, Y. Gao, M. Wu, R. Zhou, D. Chung and G. Caraveo, *et al.*, Acoustofluidic stick-and-play micropump built on foil for single-cell trapping, *Lab Chip*, 2019, **19**(18), 3045–3053.